A multidomain multigrid pseudospectral method for incompressible flows

Wenqian Chen, Yaping Ju & Chuhua Zhang

Published online: 19 Oct 2018.

Submit your article to this journal

View Crossmark data

Taylor & Francis
Taylor & Francis Group

Check for updates

A multidomain multigrid pseudospectral method for incompressible flows

Wenqian Chen[a], Yaping Ju[a], and Chuhua Zhang[a,b]

[a]Department of Fluid Machinery and Engineering, School of Energy and Power Engineering, Xi'an Jiaotong University, Xi'an, Shaanxi, People's Republic of China; [b]State Key Laboratory for Strength and Vibration of Mechanical Structures, Xi'an Jiaotong University, Xi'an, Shaanxi, People's Republic of China

ABSTRACT

Pseudospectral method has the merit of high accuracy and the defects of simple geometry suitability and low computational efficiency. To remedy the two defects, a multidomain multigrid Chebyshev pseudospectral method is proposed and validated through the numerical solution of two-dimensional incompressible Navier-Stokes equations in the primitive variable formulation. To facilitate the implementation of the multidomain multigrid method, the IP_N-IP_N method is utilized to approximate the velocity and pressure with the same degree of Chebyshev polynomials within each subdomain, and an interface/boundary condensation method is developed to implement the pseudospectral operators of multigrid at the interface/boundary of subdomains. The accuracy and efficiency of the proposed method are first validated by numerical solutions of the lid-driven cavity problem. The numerical results are in good agreement with the benchmark solutions, and the speeding up of multigrid is 4–9 compared against the single grid. Then the capability of the proposed method for even more complex geometries with a close/open boundary is demonstrated by numerical solutions of several typical problems. The proposed method is quite generic and can be extended to the high accuracy and efficiency solution of three-dimensional incompressible/compressible, unsteady/steady fluid flows and heat transfer problems.

1. Introduction

High accuracy and high-efficiency numerical methods play an increasingly important role in many theoretical and practical areas, such as high fidelity simulations of turbulent flows and heat transfer, acoustic generation and acoustic propagation, and robust design optimization of aircraft and propulsion system, etc [1]. Among various high accuracy numerical methods for Navier-Stokes equations, the pseudospectral method has an outstanding merit of exponential order accuracy with grid points and thus, has been attracting much attention of researchers during the past decades [2]. So far, the two crucial obstacles to hamper the further application of the pseudospectral method in theoretical and practical areas are its relative weak capability of dealing with complex geometry and its relatively low computational efficiency due to global nature.

To tackle the complex geometry, a number of researchers [3–5] developed the multidomain pseudospectral method by which the original complex domain is first decomposed into several relatively simple subdomains, and then each subdomain is further solved by the pseudospectral

---

CONTACT Chuhua Zhang ✉ chzhang@mail.xjtu.edu.cn 🖂 Department of Fluid Machinery and Engineering, School of Energy and Power Engineering, Xi'an Jiaotong University, No. 28 West Xianning Road, Xi'an 710049, Shaanxi, People's Republic of China.

<div style="border:1px solid black">

Nomenclature

A	coefficient matrix of interface/boundary equations	u, v	velocity components along x and y directions, respectively
a, b, h	parameters for boundary condition	**V**	velocity vector
c	correction values of unknowns on coarser grid	x, y	dimensionless Cartesian coordinates
		β	artificial compressibility coefficient
I	restriction operator for residual and unknowns	θ	dimensionless temperature
		τ	pseudo time
M, N	maximum degree of Chebyshev polynomials along x and y directions, respectively	ϕ	unknowns
		Superscripts	
		n	pseudo time step
n	unit normal vector	Ω_l	the lth subdomain
P	prolongation operator for the correction	$\partial\Omega$	interface/boundary
p	dimensionless pressure	**Subscripts**	
Pr	Prandtl number	i, j	indices of collocation points along x and y directions, respectively
R	residuals on interior points		
R'	residuals on interface/boundary	k	grid level
Re	Reynolds number	l	index of subdomain

</div>

method. One of the key issues of the multidomain pseudospectral method is how to design and implement the artificial interface conditions while keeping the pseudospectral accuracy. Zhang et al. [6] proposed a unified interface/boundary value updating algorithm for the multidomain pseudospectral solution of Navier-Stokes equations in the vortex-velocity formulation. This algorithm was found to extend the easily available single domain codes to the multidomain ones while holding the high accuracy of the pseudospectral method. Inspired by these findings, we shall propose a multidomain pseudospectral method for Navier-Stokes equations in the primitive variable formulation, which is more suitable to general fluid flows and heat transfer problems than that in the vortex-velocity formulation.

When solving Navier-Stokes equations in primitive variable formulation with the pseudospectral method, it is crucial to prevent the well-known spurious pressure mode from contaminating the flow fields [2]. So far, three kinds of strategies were developed to eliminate the spurious pressure mode, that is, staggered grid [2], IP_N-IP_{N-2} method [2,7], and IP_N-IP_N method [2,8–11]. In the staggered grid, the velocity and pressure are defined on different grids. The staggered grid can be implemented easily for one-dimensional problems, but quite difficult for two- and three-dimensional cases. In IP_N-IP_{N-2} method, the pressure is approximated with a polynomial of degree two less than the velocity. The IP_N-IP_{N-2} can effectively eliminate the spurious pressure mode for the single-domain pseudospectral method, but is less suitable for the multidomain pseudospectral method due to the lack of pressure interface/boundary conditions. In IP_N-IP_N method, the pressure and velocity are located at the same grid points and approximated with the polynomial of the same degree. With a careful design of pressure boundary condition [12], the IP_N-IP_N can be used to eliminate the spurious pressure mode for the single domain pseudospectral method. However, the suitability of IP_N-IP_N to the multidomain pseudospectral method remains unknown.

To speed up the solution convergence of numerical methods, the multigrid method is proven to yield a significant speedup for the numerical solutions of both the linear and nonlinear partial differential equations, especially, for finite difference method and finite volume method. However, quite a few works were carried out for the multigrid pseudospectral solutions of Navier-Stokes equations, and most of the available works were devoted to simple geometry, e.g., lid-driven cavity problem [7,13] and thermally driven cavity problem [14]. The suitability and performance of the multigrid pseudospectral method for complex geometry remain unknown. For complex geometry, where the aforementioned multidomain method is applied, the unknowns on interior points are solved using the governing equations while the unknowns on interface points are

solved using the interface transfer conditions. This renders the design of multigrid operators much more complex for the multidomain cases than the single domain cases. To this end, Haupt et al. [15] recently proposed an interface/boundary condensation method for the design and implementation of multigrid operators under the framework of spectral element method [15]. The basic idea behind their work is that the updating of unknowns on interface/boundary is adequate due to the elliptic character of the Helmholtz equation. Inspired by the work of Haupt et al. [15], we shall develop an interface/boundary condensation method for the multidomain multigrid operators under the framework of the pseudospectral method. Through condensing the interface/boundary equations on the finest grid, the unknowns at the interface/boundary are updated only on the finest grid while not on the coarser grids.

In the present work, in order to extend the pseudospectral method towards complex geometry and high computational efficiency, a multidomain multigrid pseudospectral method is proposed for solving Navier-Stokes equations in the primitive variable formulation. The accuracy and efficiency of the proposed method is validated by lid-driven cavity problem. Then the capability of the proposed method for even more complex geometries with close/open boundary is demonstrated by three typical problems: lid-driven cavity flow with an obstacle, backward facing step flow, and forced-convection heat transfer over a hot square cylinder.

The paper is organized as follows. In Section 2, the governing equations and boundary conditions are outlined. In Section 3, a multidomain pseudospectral method is proposed, and then a multigrid strategy for the multidomain pseudospectral is introduced in Section 4. Section 5 presents the validation of the proposed method in terms of numerical accuracy and efficiency, and Section 6 explains the further applications of the proposed method in several two-dimensional fluid flows and heat transfer problems. Some conclusions are drawn in Section 7.

2. Governing equations and boundary conditions

2.1. Governing equations

The governing equations for two-dimensional incompressible flows are written in nondimensional primitive variables formulation:

$$\nabla \cdot \mathbf{V} = 0$$
$$(\mathbf{V} \cdot \nabla)\mathbf{V} = -\nabla p + \frac{1}{\mathrm{Re}} \nabla^2 \mathbf{V} \tag{1}$$

where $\mathbf{V} = (u, v)$ is dimensionless velocity in Cartesian coordinate (x, y), p is dimensionless pressure, Re is the Reynolds number, and ∇ is the Hamiltonian operator.

2.2. Artificial compressibility equations

One of the challenges in solving the incompressible Navier-Stokes equations in the primitive variable formulation is that the incompressible continuity equation does not explicitly include the pressure term. The artificial compressibility method (ACM), in which the incompressible continuity equation is replaced by a pseudo artificial compressibility equation, was found to be an easy and efficient method for incompressible flow problems [16–18]. By introducing a pseudo time derivative term, the steady governing Eq. (1) is converted into:

$$\frac{\partial p}{\beta \partial \tau} + \nabla \cdot \mathbf{V} = 0$$
$$\frac{\partial \mathbf{V}}{\partial \tau} + (\mathbf{V} \cdot \nabla)\mathbf{V} = -\nabla p + \frac{1}{\mathrm{Re}} \nabla^2 \mathbf{V} \tag{2}$$

where τ is pseudo time, β is artificial compressibility coefficient and chosen to be 1.25 as adopted in reference [19]. As the pseudo time derivative term $\partial p/\partial \tau$, $\partial u/\partial \tau$, and $\partial v/\partial \tau$ tends to zero, the Eq. (2) turns into Eq. (1).

2.3. Boundary conditions

Under the framework of IP_N-IP_N method as stated in the next section, the pressure on boundary collocation points needs to be solved unless specified explicitly. To tackle this problem, the normal momentum equation deduced from Eq. (1) is employed as a boundary condition for pressure.

$$\frac{\partial p}{\partial \mathbf{n}} = \mathbf{n} \cdot \left((\mathbf{V} \cdot \nabla)\mathbf{V} - \frac{1}{Re}\nabla^2\mathbf{V} \right) \tag{3}$$

where, $\mathbf{n}$ is the unit normal vector of the boundary. The original form of the diffusive term $\nabla^2\mathbf{V}$ is more prone to instability because this form cannot enforce the constraint $\nabla \cdot \mathbf{V} = 0$ at the boundary. We turn to another equivalent form (4) for the diffusive term [2].

$$\nabla^2\mathbf{V} = \nabla(\nabla \cdot \mathbf{V}) - \nabla \times (\nabla \times \mathbf{V}) = -\nabla \times (\nabla \times \mathbf{V}) \tag{4}$$

Substituting Eq. (4) into Eq. (3), the boundary condition for pressure will be recast as:

$$\frac{\partial p}{\partial \mathbf{n}} = \mathbf{n} \cdot \left((\mathbf{V} \cdot \nabla)\mathbf{V} + \frac{1}{Re}\nabla \times (\nabla \times \mathbf{V}) \right) \tag{5}$$

The Dirichlet or Neumann boundary condition is employed for velocity and temperature. Combining with the boundary condition for pressure (5), we denote the boundary conditions for unknowns $\phi = (p, u, v)$ by a general formulation:

$$a\partial\phi/\partial n + b\phi = h \tag{6}$$

where, a, b, h are undetermined parameters related to a specific problem. $a = 0$ and $b \neq 0$ denotes the Dirichlet boundary condition, $a \neq 0$ and $b = 0$ Neumann boundary condition, and $a \neq 0$ and $b \neq 0$ Robin boundary condition. For periodic boundary condition, the physical boundary can be transformed to an artificial internal interface that can be treated with the multidomain method stated in next section.

3. Multidomain pseudospectral method

3.1. Pseudospectral discretization

Compared against IP_N-IP_{N-2}, the IP_N-IP_N collocation is more suitable for the multidomain and multigrid method. In the IP_N-IP_N method, the unknowns $\phi = (p, u, v)$ can be approximated with truncated Chebyshev series with the same degree,

$$\phi(x, y) = \sum_{m=0}^{M} \sum_{n=0}^{N} \hat{\phi}_{mn} T_m(x) T_n(y) \tag{7}$$

where, $T_m(x)$ is one-dimensional Chebyshev polynomial of the first kind,

$$T_m(x) = \cos(m\cos^{-1}x) \tag{8}$$

$T_n(y)$ can be written in a similar way to Eq. (8). M and N are the maximum degree of these polynomials along the x and y directions, respectively, $\hat{\phi}_{mn} = (\hat{p}, \hat{u}, \hat{v})$ is the expansion coefficient of each mode (m, n). On the dimensionless domain $[-1, 1]$, the unknowns are discretized on Chebyshev–Gauss–Lobatto points.

$$(x_i, y_j) = \left(\cos\left(\frac{\pi i}{M}\right), \cos\left(\frac{\pi j}{N}\right) \right) \qquad 0 \leq i \leq M, \ 0 \leq j \leq N \tag{9}$$

The first- and second-order derivative of the unknowns can be obtained explicitly by differentiating Eq. (7). Actually, the derivatives of unknowns are a weighted average of the unknowns in

the same direction. Taking x direction as an example, the resultant derivatives are as follows:

$$\frac{\partial \phi}{\partial x}\big|_{x_i} = \sum_{g=0}^{M} D_{i,g}^{(1)} \phi(x_g)$$

$$\frac{\partial^2 \phi}{\partial x^2}\big|_{x_i} = \sum_{g=0}^{M} D_{i,g}^{(2)} \phi(x_g) \tag{10}$$

After a series of complex but normal triangular function calculations, the coefficient matrix $\mathbf{D}^{(1)}$ for the first-order derivative is recast as:

$$\begin{cases} D_{0,0}^{(1)} = -D_{M,M}^{(1)} = -\dfrac{2M^2 + 1}{6} \\[4mm] D_{m,n}^{(1)} = \dfrac{B_m}{B_n} \dfrac{(-1)^{m+n}}{2 \sin\left[\dfrac{(m+n)\pi}{2M}\right] \sin\left[\dfrac{(n-m)\pi}{2M}\right]} \qquad 0 \leq m, n \leq M, m \neq n \\[6mm] D_{m,m}^{(1)} = -\sum_{n=0, n \neq m}^{M} D_{m,n}^{(1)} \qquad\qquad 1 \leq m \leq M-1 \\[4mm] B_m = \begin{cases} 2 & m = 0, M \\ 1 & m = 1, \dots, M-1 \end{cases} \end{cases} \tag{11}$$

The coefficient matrix $\mathbf{D}^{(2)}$ for the second-order derivative is:

$$D_{m,n}^{(2)} = \sum_{g=0}^{M} D_{m,g}^{(1)} D_{g,n}^{(1)} \tag{12}$$

As a kind of collocation method, the Chebyshev pseudospectral method forces the numerical solution to satisfy the governing equations exactly at collocation points. Therefore, by substituting Eqs. (7)–(12) into Eq. (2), we have the semi-discretized equations for Eq. (2) and denote them as:

$$\frac{\partial \phi_{i,j}}{\partial \tau} = R_{i,j} \qquad 1 \leq i \leq M-1, \ 1 \leq j \leq N-1 \tag{13}$$

where, $R_{i,j}$ is the residual of Eq. (2).

$$R_{i,j} = \begin{pmatrix} -\beta \nabla \cdot V \\ -\nabla p + \dfrac{1}{\mathrm{Re}} \nabla^2 V - (V \cdot \nabla)V \end{pmatrix}_{i,j} \tag{14}$$

3.2. Multidomain method

The multidomain method is a divide-and-conquer technique by which the whole complex domain is firstly divided into a set of simple subdomains and then each subdomain is conquered by a suitable method. The key to the multidomain method is how to cope with the artificial interface of adjacent subdomains. Figure 1(a) shows a schematic of the grid of the whole computational domain which is decomposed into 3×3 subdomains. Earlier, the authors have proposed an interface/boundary value updating method to deal with the coupling of the subdomains for solving the Navier-Stokes equations in the vorticity-velocity form [6]. The basic idea is that the value and first-order derivative of unknowns are continuous across the interface. The continuity of unknowns is satisfied automatically, as the collocation point on the interface is identical for adjacent subdomains. The continuity of the first-order derivative can be expressed as:

$$\frac{\partial \phi}{\partial \mathbf{n}^+} = \frac{\partial \phi}{\partial \mathbf{n}^-} \tag{15}$$

where the two sides of equation denote the derivatives obtained from both sides of the interface.

Combining the artificial interface condition (15) with physical boundary condition (6), we have the general interface/boundary equations.

$$\begin{cases} \dfrac{\partial \phi}{\partial \mathbf{n}^+} = \dfrac{\partial \phi}{\partial \mathbf{n}^-}, & \text{on artifical interface} \\ a\dfrac{\partial \phi}{\partial \mathbf{n}} + b\phi = h, & \text{on physical boundary} \end{cases} \tag{16}$$

Taking x direction as an example, the computational domain is divided into L subdomains $\Omega_l = [x_l, x_{l+1}]$ with M_l collocation points $[\phi_{l-1}^{\partial\Omega}, \phi_1^{\Omega_l}, ... \phi_{M_l-1}^{\Omega_l}, \phi_l^{\partial\Omega}]$, $l = 1, 2, ..., L$. Substituting Eq. (10) into Eq. (15) leads to the following equation on the interface x_l:

$$D_{M_l,0}^{\Omega_l}\phi_{l-1}^{\partial\Omega} + \sum_{g=1}^{M_l-1} D_{M_l,g}^{\Omega_l}\phi_g^{\Omega_l} + D_{M_l,M_l}^{\Omega_l}\phi_l^{\partial\Omega}$$

$$= D_{0,0}^{\Omega_{l+1}}\phi_l^{\partial\Omega} + \sum_{g=1}^{M_{l+1}-1} D_{0,g}^{\Omega_{l+1}}\phi_g^{\Omega_{l+1}} + D_{0,M_{l+1}}^{\Omega_{l+1}}\phi_{l+1}^{\partial\Omega} \tag{17}$$

Thus, we have the interface/boundary discretized equations for Eq. (16)

$$\mathbf{A} \cdot \mathbf{x} = \mathbf{s} \tag{18}$$

with the unknown vector $\mathbf{x} = [\phi_0^{\partial\Omega}, \phi_1^{\partial\Omega}, ..., \phi_L^{\partial\Omega}]$. The coefficient matrix $\mathbf{A}$ and the source term $\mathbf{s}$ are:

$$\mathbf{A} = \begin{vmatrix} aD_{M_1,0}^{\Omega_1} + b & aD_{M_1,M_1}^{\Omega_1} \\ D_{M_1,0}^{\Omega_1} & D_{M_1,M_1}^{\Omega_1} - D_{0,0}^{\Omega_2} & D_{0,M_2}^{\Omega_2} \\ & & \cdots \\ & & D_{M_{L-1},0}^{\Omega_{L-1}} & D_{M_{L-1},M_{L-1}}^{\Omega_{L-1}} - D_{0,0}^{\Omega_L} & D_{0,M_L}^{\Omega_L} \\ & & & aD_{0,0}^{\Omega_L} & aD_{0,0}^{\Omega_L} + b \end{vmatrix} \tag{19}$$

$$\mathbf{s} = \begin{vmatrix} h - a\displaystyle\sum_{g=1}^{M_1-1} D_{0,g}^{\Omega_1}\phi_g^{\Omega_1} \\ \displaystyle\sum_{g=1}^{M_2-1} D_{0,g}^{\Omega_2}\phi_g^{\Omega_2} - \sum_{g=1}^{M_1-1} D_{M_1,g}^{\Omega_1}\phi_g^{\Omega_1} \\ \cdots \\ \displaystyle\sum_{g=1}^{M_L-1} D_{0,g}^{\Omega_L}\phi_g^{\Omega_L} - \sum_{g=1}^{M_{L-1}-1} D_{M_{L-1},g}\phi_g^{\Omega_{L-1}} \\ h - a\displaystyle\sum_{g=1}^{M_L-1} D_{0,g}^{\Omega_L}\phi_g^{\Omega_L} \end{vmatrix} \tag{20}$$
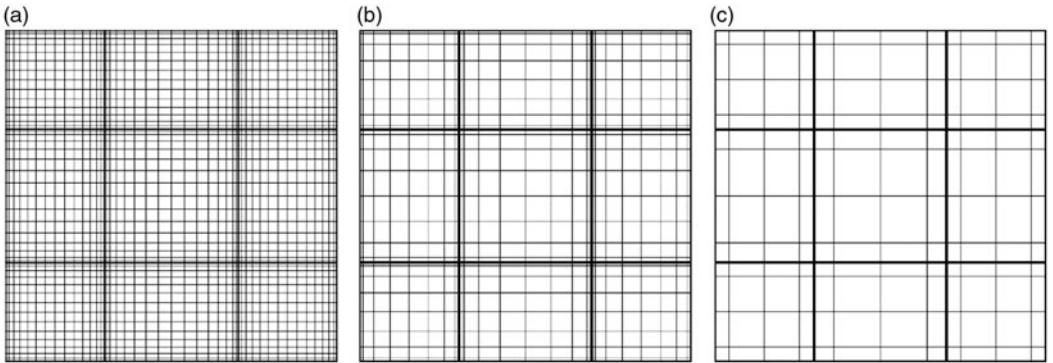

Figure 1. Schematic of three multidomain computational grids: (a) Fine grid; (b) Middle grid; (c) Coarse grid.

Equation (18) is recast as the following equation for the increment of unknowns.

$$\begin{cases} \mathbf{A} \cdot \Delta\mathbf{x} = R' = \mathbf{s} - \mathbf{A} \cdot \mathbf{x}_0 \\ \qquad \mathbf{x} = \mathbf{x}_0 + \Delta\mathbf{x} \end{cases} \qquad (21)$$

$\mathbf{x}_0$ is an approximation of $\mathbf{x}$, and R' is corresponding residual on the interface/boundary. The resultant algebraic Eq. (21) is directly solved by Tri-Diagonal Matrix Algorithm (TDMA).

3.3. Pseudo time marching scheme

Pseudo time marching method is an effective method to numerically solve the time-independent nonlinear problems. It is applied to Eq. (13) to update ϕ iteratively. The marching procedure in each pseudo time step consists of two steps. First, the unknowns on interior points of all subdomains are updated from ϕ^n to ϕ^{n+1}, while the unknowns on the interface/boundary are kept at ϕ^n. Second, the unknowns on interface/boundary are updated from ϕ^n to ϕ^{n+1}, while the unknowns on the interior points of all subdomains are kept at ϕ^{n+1}. The global solution procedure is as follows:

(1) For updating unknowns on interior points (x_i, y_j) in each subdomain, the explicit four-stage fourth-order Runge-Kutta method is employed for pseudo time marching from ϕ^n to ϕ^{n+1}.

$$\begin{aligned} \phi_{i,j}^{(1)} &= \phi_{i,j}^n + \frac{1}{4}\Delta\tau R_{i,j}^n \\ \phi_{i,j}^{(2)} &= \phi_{i,j}^n + \frac{1}{3}\Delta\tau R_{i,j}^{(1)} \\ \phi_{i,j}^{(3)} &= \phi_{i,j}^n + \frac{1}{2}\Delta\tau R_{i,j}^{(2)} \\ \phi_{i,j}^{n+1} &= \phi_{i,j}^n + \Delta\tau R_{i,j}^{(3)} \end{aligned} \qquad (22)$$

The pseudo time step $\Delta\tau$ is given explicitly according to stability analysis [20].

$$\begin{aligned} \Delta\tau &= \frac{\text{CFL}}{\lambda_x + \lambda_y} \\ \lambda_x &= \frac{|u_{\max}| + \sqrt{u_{\max}^2 + \beta^2}}{\Delta x} + \frac{1}{\text{Re} \cdot \Delta x^2} \\ \lambda_y &= \frac{|v_{\max}| + \sqrt{v_{\max}^2 + \beta^2}}{\Delta y} + \frac{1}{\text{Re} \cdot \Delta y^2} \end{aligned} \qquad (23)$$

where, CFL is the Courant-Friedrichs-Lewy number, Δx and Δy are the minimum grid spacing along x and y directions, respectively, and $u_{\max}$ and $v_{\max}$ denote the maximum velocity.

(2) For updating unknowns on interface/boundary, we first sweep the horizontal gridline, and solve Eq. (21) successively for updating unknowns on the horizontal interface/boundary. Then we sweep vertical gridline, and solve Eq. (21) successively for updating unknowns on the vertical interface/boundary. When solving Eq. (21), the unknowns ϕ^n on interface/boundary are set as the approximation of ϕ^{n+1}.

4. Multigrid for multidomain pseudospectral method

4.1. Multigrid method

The conventional iterative method can fast damp the high-frequency error, but becomes inefficient for the low-frequency error. Whether it is high-frequency error or not, is related to the grid spacing. Low-frequency error on fine grid becomes high-frequency error on coarser grids, and it

can be damped rapidly on the coarser grids. Based on this observation, the multigrid method was proposed and proven efficient for a variety of iterative methods [13, 14]. In the author's early work, the multigrid method was proved very efficient in accelerating convergence for a single domain pseudospectral method [7]. In this paper, we extend the multigrid method to the multi-domain pseudospectral case to improve the computational efficiency.

Taking V-cycle multigrid as an example, three grid levels: fine, middle and coarse grid are denoted by $k = 1$, 2 and 3, respectively. The variable with subscript k denotes that defined on grid level k. The distribution of collocation points of each subdomain on the grid level k and $k-1$ satisfies $M_k = 2M_{k-1}, N_k = 2N_{k-1}$. The schematic of these three grids is shown in Figure 1. The procedure of V-cycle multigrid is given in Figure 2. In the multidomain pseudospectral method, the unknowns on interior points and interface/boundary are updated by Eqs. (22) and (21), respectively. Compared to the single domain multigrid method, it is relatively complicated to design the operators of multigrid for the multidomain pseudospectral method. Inspired by reference [15], an interface/boundary condensation method is developed to implement the operators of multigrid. The basic idea is that the interface/boundary transfer condition (21) implies an explicit dependency between the unknowns on artificial interface/boundary and interior points; therefore, the updating of unknowns on interface/boundary on the finest grid is adequate, while those on coarser grids will even produce an error. It can be fulfilled by updating of interface/boundary only on grid level $k = 1$ in the smoothing process.

4.2. Multigrid operators

The full approximation scheme (FAS), which is suitable to the nonlinear equations, is adopted to construct the multigrid operators for the discretized Eq. (22). As discretized equations on the coarser grid cannot represent exactly those on a finer grid, it is critical to construct the defect equations of the original discretized equations on the coarser grid. The discretized equations to be solved on each grid level are denoted as

$$R_k(\phi) = r_k = \begin{cases} 0, & k = 1 \\ d_k, & k = 2, 3 \end{cases} \tag{24}$$

Here, d_k denotes the additional term of the defect equations on the coarser grid.

$$d_k = I_{k-1}^k(R_{k-1}) - R_k\left(I_{k-1}^k(\phi_{k-1})\right) \tag{25}$$

where, $I_{k-1}^k(R_{k-1})$ and $I_{k-1}^k(\phi_{k-1})$ are restriction operators for residuals and unknowns, respectively, from grid level $k-1$ to k. The V-cycle multigrid operators including smoothing, restriction, and prolongation operator are shown in Figure 2 and defined as follows:
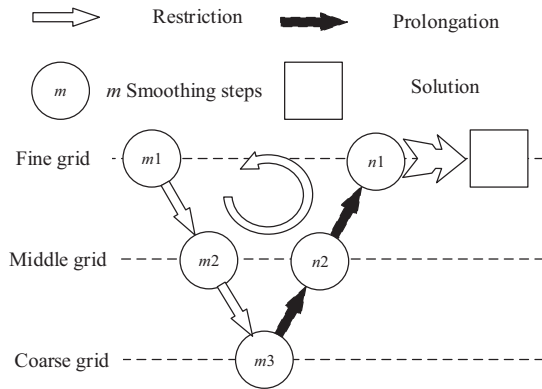

Figure 2. The process of three-level V-cycle multigrid.

4.2.1. Smoothing operator

The pseudo time marching scheme is used for smoothing the unknowns. On the grid level $k = 1$, both the unknowns on interior points and interface/boundary are updated. On the grid level $k = 2$, 3, only the unknowns on interior points are updated, while the unknowns on interface/boundary are not updated.

4.2.1.1. $\phi_k = I^k_{k-1}(\phi_{k-1})$: restriction operator for unknowns from grid level $k-1$ to k.
According to Eq. (9), the collocation points on the grid level k are the subset of those on the grid level $k-1$. Therefore, the restriction of unknowns is accomplished by direct injection:

$$(\phi_k)_{i,j} = (\phi_{k-1})_{2i,2j} \qquad\qquad i = 0, ..., M_k, j = 0, ..., N_k \qquad (26)$$

4.2.1.2. $R_k = I^k_{k-1}(R_{k-1})$: restriction operator for residuals from grid level $k-1$ to k.
The restriction operator for residuals is implemented through a low-pass filter in the Chebyshev spectral space. In each subdomain, the residual is first transformed from physical space to the Chebyshev spectral space; second, the high-frequency component is removed; third, the resulting residual is transformed back from the Chebyshev spectral space to the physical space. Besides, as the unknowns on interior pints in each subdomain are updated with Dirichlet-Dirichlet boundary condition, the residuals on interface/boundary are set zeroes before the implementation of restriction. Taking x direction as an example, the process of restriction for residuals is organized as follows:

$$(R_{k-1})_0 = (R_{k-1})_{M_{k-1}} = 0$$
$$(\hat{R}_{k-1})_m = \frac{2}{M_{k-1}B_m} \sum_{i=0}^{M_{k-1}} \frac{1}{B_i}(R_{k-1})_i \cos\left(\frac{\pi i m}{M_{k-1}}\right) \qquad m = 0, 1, ..., M_{k-1}$$
$$(\hat{R}_{k-1})_m = 0 \qquad\qquad m = M_k + 1, ..., M_{k-1}$$
$$(R_k)_i = \sum_{m=0}^{M_k}(\hat{R}_{k-1})_m \cos\left(\frac{\pi i m}{M_k}\right) \qquad i = 0, 1, ..., M_k \qquad (27)$$

4.2.1.3. $c_k = P^k_{k+1}(c_{k+1})$: prolongation operator for the correction of unknowns from grid level k to $k-1$.
In the full approximation scheme (FAS), the purpose of the prolongation operator is to remove the low-frequency error while not increasing the high-frequency error on the finer grid. Therefore, the correction of unknowns is prolonged from grid level k to $k-1$.

For the interior points, the prolongation operator is similar to the restriction operator for residual. The basic idea is that: in each subdomain, the correction is first transformed from the physical space to the Chebyshev spectral space; second, the resulting correction is transformed from the Chebyshev spectral space to the physical space. Taking x direction as an example, the process of prolongation for corrections is organized as follows:

$$(\hat{c}_k)_m = \frac{2}{M_k B_m} \sum_{i=0}^{M_k} \frac{1}{B_i}(c_k)_i \cos\left(\frac{\pi i m}{M_k}\right) \qquad m = 0, 1, ..., M_k$$
$$(c_{k-1})_i = \sum_{m=0}^{M_k}(\hat{c}_k)_m \cos\left(\frac{\pi i m}{M_{k-1}}\right) \qquad i = 0, 1, ..., M_{k-1} \qquad (28)$$

5. Validation

In this section, the accuracy and the efficiency of the proposed method are validated against the benchmark solutions for the two-dimensional lid-driven cavity problem. The flow is driven by

the moving top wall, as shown in Figure 3. The well-known difficulty of this problem is the corner singularity, which is caused by the discontinuity of horizontal velocity at the two top corners. In order to remove the singularity, the speed of moving wall is defined as $V_w = 16x^2(1-x)^2$ as adopted in references [21–23]. The other walls are treated with no-slip boundary condition. The pressure boundary condition is defined by Eq. (5).

The whole computational domain is decomposed into 3×3 regular subdomains. In each subdomain, the number of collocation points is set as 17×17 on grid level $k = 1$. The iteration is accelerated with the aforementioned three-level V-cycle multigrid. After the converged solution is obtained, the solutions on collocation points are interpolated into a uniform grid of 500×500 using the Chebyshev spectral function.

Streamlines at different Reynolds numbers are shown in Figure 4. As Reynolds number increases, the primary vortex gradually moves to the center of the cavity; both the two bottom secondary vortexes become larger and move to the center of the cavity too. Table 1 lists a quantitative comparison of the present results with the benchmark results [21–23] for the positions of the primary vortex and secondary vortices at different Reynolds numbers. These results are in good agreement with the benchmarks, verifying the accuracy of the present method.

Both the single grid and multigrid computations are performed to check the speedup of the multigrid method. The computations on the single grid are performed on the grid level $k = 1$. In contrast, the computations on the multigrid are performed using three-level V cycles as shown in Figure 2. Figure 5 presents the residual *versus* CPU time for the three-level V-cycle multigrid and single grid, respectively. Some interesting findings are observed. First, whether in a single grid or three-level V-cycle multigrid, the CPU time consumed for convergence increases with Reynolds number. This is due to the complex flow pattern as the convection is enforced. Second, the dropping rate of the residual in multigrid is much larger with lower oscillation than that in the single grid. This finding reflects that the low-frequency error can be damped effectively in multigrid. Third, the speedup factors by multigrid are 9.39, 7.55, 6.43, 3.63 at Reynolds numbers 100, 200, 400, 1,000. The speedup factor decreases as Reynolds number increases, reflecting the increasing nonlinear effect.

6. Results and discussion

6.1. Lid-driven cavity problem with square obstacle

To demonstrate the capability of the proposed method in dealing with the real multidomain flow, we insert an obstacle into the above lid-driven cavity and study the influence of the obstacle on the flow. The obstacle (black domain) of different positions and the corresponding multidomain partitions (dashed lines) are shown in Figure 6. In each subdomain, the number of collocation points is set as 17×17 on grid level $k = 1$. The speed of moving wall is defined as
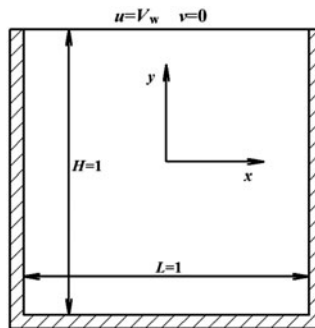

Figure 3. The geometry and dimensions of lid-driven cavity flow.

$V_w = 16x^2(1-x)^2$. The other walls of the cavity and the walls of the obstacle are implemented with no-slip boundary condition. The pressure boundary condition is defined by Eq. (5).

Figure 7 shows the streamlines of lid-driven cavity flow with the obstacle of different positions. Comparison of these streamlines with Figure 4(d) shows that the existence of obstacle has great influence on the vortexes in the cavity. When the obstacle is located at the center of the cavity, the primary vortex moves to the top left; a small vortex arises at the bottom of the obstacle; two bottom secondary vortex are nearly unchanged. When the obstacle is located at the bottom left corner of the cavity, both the two bottom secondary vortexes become stronger. When the obstacle is located at the bottom right corner of the cavity, the bottom left secondary vortex size is increased, while the bottom right secondary vortex size is reduced.

6.2. Backward-facing step flow

To demonstrate the capability of the proposed method in handing the flow separation and the open inlet/outlet boundary conditions, the backward-facing step flow is studied. The geometry and boundary conditions are shown in Figure 8. The geometry is identical to that in Gartling [24] and has a channel height H, a step height $H/2$ at the inlet, and a channel length $L = 30H$. The channel length is sufficient to produce a fully developed flow at the outlet. In the non-dimensionalization, the characteristic length is inlet height H, and the characteristic velocity is the
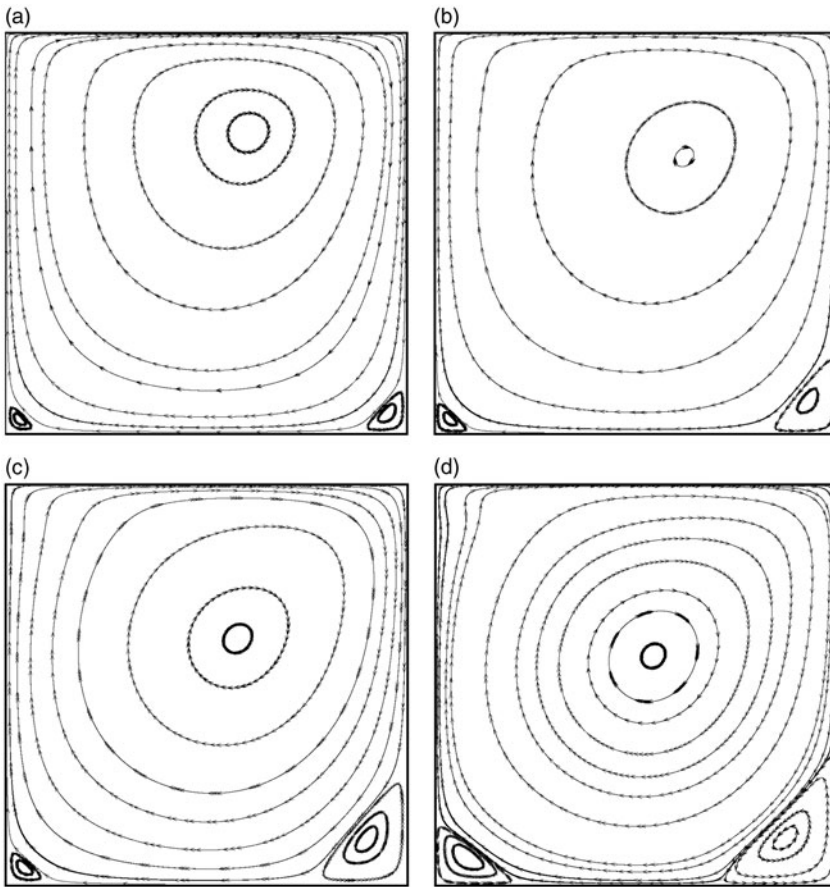

Figure 4. Streamlines of lid-driven cavity flow: (a) Re = 100; (b) Re = 200; (c) Re = 400; (d) Re = 1,000.

Table 1. Vortex positions of the two-dimensional lid-driven cavity problem. The two values for each entry refer to x coordinate and y coordinate of vortex center ($0 \leq x, y \leq 1$), respectively.

Re	Reference	Primary	Secondary right	Secondary left
100	Present	0.607, 0.754	0.952, 0.049	0.034, 0.034
100	Phillips	0.598, 0.757	0.952, 0.048	0.038, 0.038
100	Shen	0.609, 0.750	0.953, 0.047	0.031, 0.031
100	Pinelli	0.599, 0.750	0.959, 0.045	0.038, 0.038
200	Present	0.622, 0.691	0.930, 0.080	0.035, 0.035
200	Phillips	0.621, 0.691	0.929, 0.084	0.038, 0.038
200	Pinelli	0.628, 0.691	0.933, 0.087	0.038, 0.038
400	Present	0.578, 0.616	0.900, 0.114	0.045, 0.043
400	Phillips	0.573, 0.621	0.902, 0.113	0.048, 0.038
400	Shen	0.578, 0.625	0.922, 0.094	0.031, 0.047
400	Pinelli	0.565, 0.629	0.897, 0.103	0.038, 0.038
1000	Present	0.543, 0.573	0.872, 0.116	0.077, 0.069
1000	Phillips	0.549, 0.573	0.870, 0.113	0.071, 0.071
1000	Shen	0.547, 0.578	0.922, 0.094	0.078, 0.063
1000	Pinelli	0.540, 0.574	0.880, 0.114	0.067, 0.067
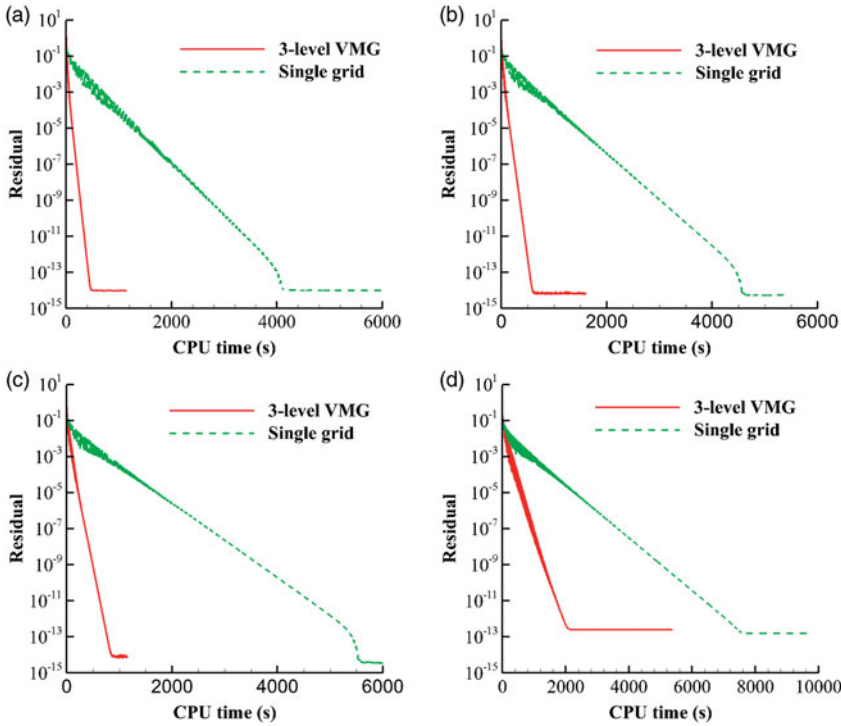
Figure 5. Residual *versus* CPU time for three-level V-cycle multigrid and single grid: (a) Re $=$ 100; (b) Re $=$ 200; (c) Re $=$ 400; (d) Re $=$ 1,000.

average inlet velocity u_{avg}. All the walls are imposed with no-slip boundary condition. The inlet velocity profile is specified as horizontal flow with a parabolic distribution.

$$u(y) = 24y(0.5 - y) \qquad\qquad 0 \leq y \leq 0.5 \qquad\qquad (29)$$

From the inlet velocity profile, the maximum inflow velocity is $u_{max} = 1.5$, and the average velocity is $u_{avg} = 1.0$. The outlet boundary condition is $\partial u/\partial x = 0$, $\partial v/\partial x = 0$. The pressure boundary condition is defined by Eq. (5).

In this case, we partition the domain into 15×2 subdomains, each of equal size 2×0.5 and 17×17 collocation points. The flow at Reynolds number 100, 200, 400, 800 are simulated, the streamlines of which are shown in Figure 9. For the sake of clarity, only the upstream flow region

of the $15H$ channel length is plotted. The vortex at the bottom wall becomes larger as Reynolds number increases. There is a critical Reynolds number (200–400), above which the vortex at the top wall arises and becomes larger as Reynolds number increases. Further, the critical Reynolds number is about 300 as shown in Erturk's [25] study. The positions of the vortexes at the bottom and top wall values are compared with those obtained by previous work as given in Table 2. The present results show a good agreement with those by Gartling [24].

6.3. Forced-convection heat transfer from a square cylinder

To further demonstrate the capability of the proposed method in predicting heat transfer and open inlet/outlet conditions, the forced-convection heat transfer from a square cylinder is examined in this subsection. The problem is very attractive due to complex flow regimes according to Reynolds and Prandtl numbers. For an unbounded flow across a square cylinder, the geometry is identical to that examined by Dhiman et al. [26], which is shown in Figure 10. The inlet and outlet are located $9d$ and $17d$ away from the center of square cylinder respectively. The two lateral boundaries are located symmetrically $10d$ away from the center of the square cylinder. The non-dimensional governing equations for the problem are written with an additional energy equation as follows:

$$\nabla \cdot \mathbf{V} = 0$$
$$(\mathbf{V} \cdot \nabla)\mathbf{V} = -\nabla p + \frac{1}{\mathrm{Re}}\nabla^2 \mathbf{V}$$
$$(\mathbf{V} \cdot \nabla)\theta = \frac{1}{\mathrm{Re} \times \mathrm{Pr}}\nabla^2 \theta \tag{30}$$

The last equation is a kind of convection-diffusion equation with the unknown θ as nondimensional temperature, and it is also solved numerically using the proposed method. The characteristic length for the non-dimensionalization is the square cylinder width d, while the characteristic velocity is the inflow velocity U_∞. The nondimensional temperature is defined as $\theta = (T - T_\infty)/(T_w - T_\infty)$. The boundary conditions are defined to be $u = 1.0$, $v = 0$, $\theta = 0$ at the inlet, $\partial u/\partial x = 0$, $\partial v/\partial x = 0$, $\partial \theta/\partial x = 0$ at the outlet, $\partial u/\partial y = 0$, $\partial v/\partial y = 0$, $\partial \theta/\partial y = 0$ at the lateral boundaries, and $u = 0$, $v = 0$, $\theta = 1$ on the surfaces of the square cylinder. The pressure boundary condition is defined by Eq. (5).

The heat transfer from the hot square cylinder to the cold fluid is described by Nusselt number. The local Nusselt number can be written as follows:

$$\mathrm{Nu}_l = \frac{hd}{\lambda} = -\frac{\partial \theta}{\partial \mathbf{n}} \tag{31}$$

where h is the local convective heat transfer coefficient of the flow, λ is the thermal conductivity of the fluid, and $\mathbf{n}$ is the unit outward normal vector of the square cylinder surface. The overall Nusselt number Nu can be calculated by averaging Nu_l along the square cylinder surfaces.
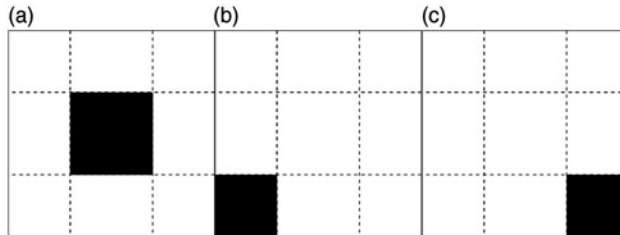

Figure 6. The geometry and multidomain partitions of lid-driven cavity flow with square obstacle: (a) Obstacle of size 0.4×0.4 located in the center; (b) Obstacle of size 0.3×0.3 located in the bottom left; (c) Obstacle of size 0.3×0.3 located in the bottom right.
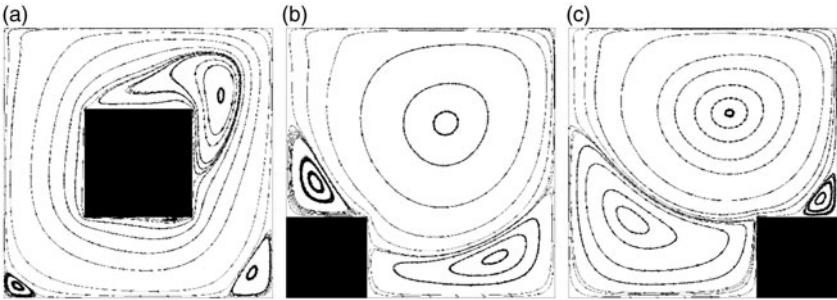
Figure 7. Streamlines of lid-driven cavity flow with square obstacle at Reynolds number 1,000: (a) Obstacle of size 0.4 × 0.4 located in the center; (b) Obstacle of size 0.3 × 0.3 located in the bottom left; (c) Obstacle of size 0.3 × 0.3 located in the bottom right.
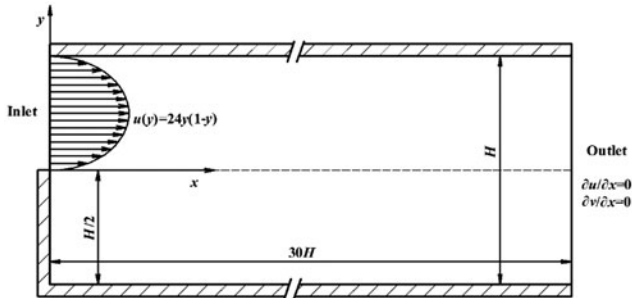

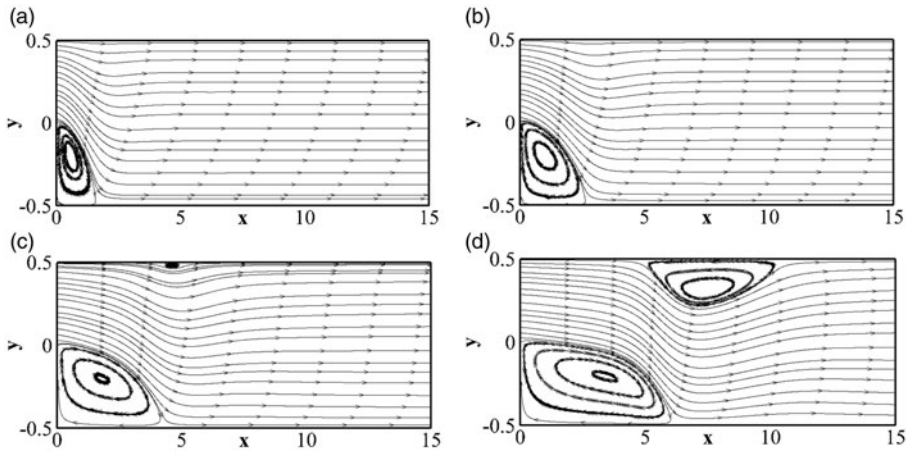**Figure 8.** Schematic of the geometry and boundary condition for backward facing step flow.

Figure 9. Streamlines of the backward facing step flow: (a) Re = 100; (b) Re = 200; (c) Re = 400; (d) Re = 800.

Table 2. Vortex positions of the backward-facing step flow at Re = 800.

	Top vortex			Bottom vortex		
Reference	P_s	P_r	L	P_s	P_r	L
Present	4.86,0.50	10.46,0.50	5.60	0.00,0.00	6.10,0.00	6.10
Gartling	4.85,0.50	10.48,0.50	5.63	0.00,0.00	6.09,0.00	6.09

P_s: separation point; P_r: reattachment point; L: length of recircculation region.

To facilitate the multidomain multigrid simulation, the domain is partitioned into 6×5 subdomains, and 25×25 collocation points are placed in each subdomain. The non-dimensional sizes of subdomains are [7.75, 1, 1, 1, 7.75, 7.75] in x direction and [8.5, 1, 1, 1, 8.5] in y direction, respectively. Figure 11 shows the multidomain partitions and the grid close to the square cylinder.

Figure 12 shows the isotherms and streamlines close to the square cylinder. Among the surfaces of the square cylinder, the front surface has the densest isotherms, indicating maximum heat transfer performance. The calculated overall Nusselt number is listed in Table 3 together with available results using various methods [8,26,27]. The present results agree well with those of Dhiman et al. [26] and Wang et al. [8], but differ up to about 4–6% with that of Paliwal et al. [27]. The discrepancy may be due to the difference in numerical methods and grid numbers.
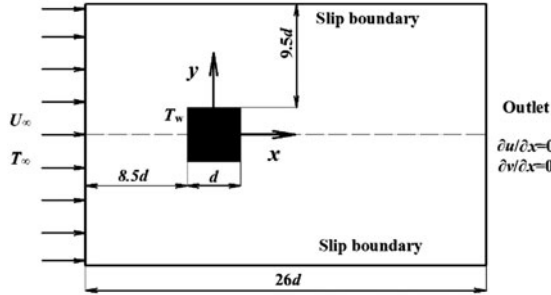

Figure 10. Schematic of the geometry and boundary condition for forced-convection heat transfer from a square cylinder.
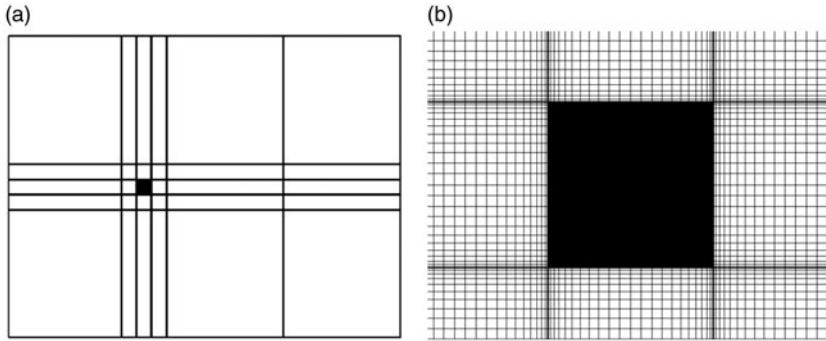

Figure 11. Computational grid for forced-convection heat transfer from a square cylinder: (a) Multidomain partitions; (b) Grid close to the square cylinder.
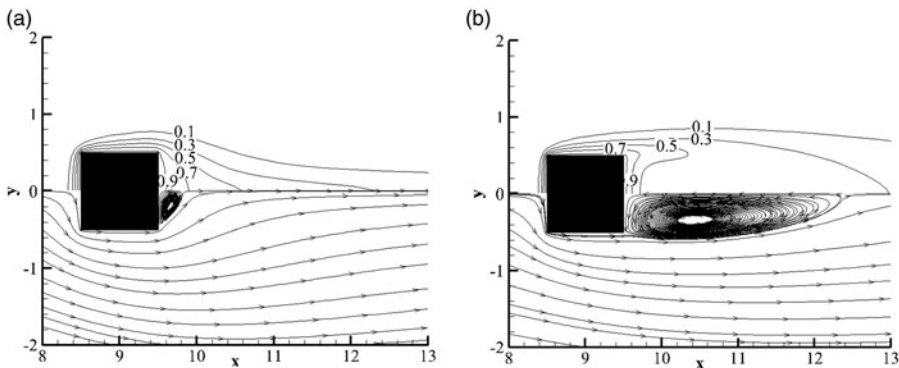

Figure 12. Isotherms (upper halves) and streamlines (lower halves) of forced-convection heat transfer from a square cylinder: (a) Re $\times$ Pr $= 5 \times 100$; (b) Re $\times$ Pr $= 40 \times 10$.

Table 3. The overall Nusselt number on the surfaces of the square cylinder. N is the number of points on each side of the square cylinder.

Reference	Methods	N	Re $\times$ Pr 5×100	40×10
Present	Pseudospectral	25	5.490	6.535
Dhiman	Finite volume	100	5.50	6.57
Wang	Pseudospectral	41	5.505	6.535
Paliwal	Finite difference	10	5.72	6.91

Paliwal used a finite difference method on a uniform staggered grid without any refinement close to the square cylinder, and the number of grid points on each side of the square cylinder is only 10. Taken the scheme accuracy and grid resolution into consideration, the present results together with those of Dhiman and Wang are believed to be more reliable than those of Paliwal.

7. Conclusions

In order to enhance the computational efficiency of the high-accuracy pseudospectral method for complex geometry, a multidomain multigrid Chebyshev pseudospectral method is proposed in this study. The IP_N-IP_N method is combined with the interface/boundary value updating the method to couple the subdomains for the numerical solutions of Navier-Stokes equations in the primitive variables formulation. A multigrid method is developed to improve the computational efficiency of the multidomain pseudospectral method. The proposed method is first validated by a lid-driven cavity problem. The numerical results show good agreement with the benchmark solutions and the speedup factor of multigrid is 4–9 compared with the single grid. Then the capability of the proposed method in predicting the fluid flow and the heat transfer is demonstrated by three typical problems: the lid-driven cavity problem with an obstacle, the backward facing step flow, and the forced-convection heat transfer from a square cylinder. On one way, the solution of these problems further show high accuracy of the present method; on the other way, it shows the capability in handing problems with complex geometry and close/open boundary. The proposed method is quite generic and can be extended to the solution of three-dimensional incompressible/compressible unsteady/steady problems.

Funding

References

[1]   Z. J. Wang, "High-order computational fluid dynamics tools for aircraft design," *Philos. Trans. A Math. Phys. Eng. Sci.*, vol. 372, no. 2022, pp. 20130318, 2014.

[2]   R. Peyret, *Spectral Methods for Incompressible Viscous Flow*. New York: Springer Verlag, 2002.

[3]   S. S. Chen, B. W. Li, and X. Y. Tian, "Chebyshev collocation spectral domain decomposition method for coupled conductive and radiative heat transfer in a 3D L-shaped enclosure," *Numer. Heat Transf. Part B Fundam.*, vol. 70, no. 3, pp. 215–232, 2016.

[4]   H. Ma, Y. Qin, and Q. Ou, "Multidomain Legendre–Galerkin Chebyshev-collocation method for one-dimensional evolution equations with discontinuity," *Appl. Numer. Math.*, vol. 111, pp. 246–259, 2017.

[5]   H. Wu, J. Pan, and H. Zheng, "Chebyshev-Legendre spectral domain decomposition method for two-dimensional vorticity equations," *Commun. Comput. Phys.*, vol. 19, no. 05, pp. 1221–1241, 2016.

[6]   C. H. Zhang, W. Zhang, and G. Xi, "A pseudospectral multidomain method for conjugate conduction-convection in enclosures," *Numer. Heat Transf. Part B Fundam.*, vol. 57, no. 4, pp. 260–282, 2010.

[7]   W. Zhang, C. H. Zhang, and G. Xi, "An explicit Chebyshev pseudospectral multigrid method for incompressible Navier-Stokes equations," *Comput. Fluids*, vol. 39, no. 1, pp. 178–188, 2010.
[8]   Z. H. Wang, Z. Huang, W. Zhang, and G. Xi, "A multidomain Chebyshev pseudo-spectral method for fluid flow and heat transfer from square cylinders," *Numer. Heat Transf. Part B Fundam.*, vol. 68, no. 3, pp. 224–238, 2015.
[9]   K. Hejranfar, and M. Hajihassanpour, "Chebyshev collocation spectral lattice Boltzmann method for simulation of low-speed flows," *Phys. Rev. E*, vol. 91, no. 1, pp. 154–173, 2015.
[10]   R. Yuan, M. Wu, and Z. Huang, "Steady mixed convective flow and heat transfer from tandem square cylinders in a horizontal channel," *Numer. Heat Transf. Part A Appl.*, vol. 71, no. 10, pp. 1023–1033, 2017.
[11]   K. Hejranfar, and M. Hajihassanpour, "Chebyshev collocation spectral lattice Boltzmann method in generalized curvilinear coordinates," *Comput. Fluids*, vol. 146, pp. 154–173, 2017.
[12]   S. A. Orszag, M. Israeli, and M. O. Deville, "Boundary conditions for incompressible flows," *J. Sci. Comput.*, vol. 1, no. 1, pp. 75–111, 1986.
[13]   M. H. Chou, "A multigrid pseudospectral method for steady flow computation," *Int. J. Numer. Methods Fluids*, vol. 43, no. 1, pp. 25–42, 2003.
[14]   K. Krastev, and M. Schäfer, "A multigrid pseudo-spectral method for incompressible Navier-Stokes flows," *C. R. Mec.*, vol. 333, no. 1, pp. 59–64, 2005.
[15]   L. Haupt, J. Stiller, and W. E. Nagel, "A fast spectral element solver combining static condensation and multigrid techniques," *J. Comput. Phys.*, vol. 255, pp. 384–395, 2013.
[16]   J. R. Clausen, "Entropically damped form of artificial compressibility for explicit simulation of incompressible flow," *Phys. Rev. E*, vol. 87, no. 1, pp. 1–12, 2013.
[17]   T. Ohwada, and P. Asinari, "Artificial compressibility method revisited: asymptotic numerical method for incompressible Navier-Stokes equations," *J. Comput. Phys.*, vol. 229, no. 5, pp. 1698–1723, 2010.
[18]   P. Asinari, T. Ohwada, E. Chiavazzo, and A. F. Di Rienzo, "Link-wise artificial compressibility method," *J. Comput. Phys.*, vol. 231, no. 15, pp. 5109–5143, 2012.
[19]   C. Liang, A. S. Chan, and A. Jameson, "A P-multigrid spectral difference method for two-dimensional unsteady incompressible Navier–Stokes equations," *Comput. Fluids*, vol. 51, no. 1, pp. 127–135, 2011.
[20]   D. Kwak, J. L. C. Chang, S. P. Shanks, and S. R. Chakravarthy, "A three-dimensional incompressible Navier-Stokes flow solver using primitive variables," *AIAA J.*, vol. 24, no. 3, pp. 390–396, 1986.
[21]   T. N. Phillips, and G. W. Roberts, "The treatment of spurious pressure modes in spectral incompressible flow calculations," *J. Comput. Phys.*, vol. 105, no. 1, pp. 150–164, 1993.
[22]   A. Pinelli, and A. Vacca, "Chebyshev collocation method and multidomain decomposition for the incompressible Navier-Stokes equations," *Int. J. Numer. Methods Fluids*, vol. 18, no. 8, pp. 781–799, 1994.
[23]   J. Shen, "Hopf bifurcation of the unsteady regularized driven cavity flow," *J. Comput. Phys.*, vol. 95, no. 1, pp. 228–245, 1991.
[24]   D. K. Gartling, "A test problem for outflow boundary conditions-flow over a backward-facing step," *Int. J. Numer. Meth. Fluids*, vol. 11, no. 7, pp. 953–967, 1990.
[25]   E. Erturk, "Numerical solutions of 2-D steady incompressible flow over a backward-facing step, part I: High Reynolds number solutions," *Comput. Fluids*, vol. 37, no. 6, pp. 633–655, 2008.
[26]   A. K. Dhiman, R. P. Chhabra, and V. Eswaran, "Heat transfer to power-law fluids from a heated square cylinder," *Numer. Heat Transf. Part A Appl.*, vol. 52, no. 2, pp. 185–201, 2007.
[27]   B. Paliwal, A. Sharma, R. P. Chhabra, and V. Eswaran, "Power law fluid flow past a square cylinder: momentum and heat transfer characteristics," *Chem. Eng. Sci.*, vol. 58, no. 23–24, pp. 5315–5329, 2003.